Energy-dependent photoemission delays from noble metal surfaces by attosecond interferometry

Locher, Reto ; Castiglioni, Luca ; Lucchini, Matteo ; Greif, Michael ; Gallmann, Lukas ; Osterwalder, Jürg ; Hengsberger, Matthias ; Keller, Ursula

DOI: https://doi.org/10.1364/OPTICA.2.000405

Energy-dependent photoemission delays from noble metal surfaces by attosecond interferometry

Supplementary Information

R. Locher,[1]* L. Castiglioni,[2]*† M. Lucchini,[1] M. Greif,[2] L. Gallmann,[1]
J. Osterwalder,[2] M. Hengsberger,[2] U. Keller[1]

[1]*Physics Department, ETH Zurich, CH-8093 Zürich, Switzerland.*
[2]*Department of Physics, University of Zurich, CH-8057 Zürich, Switzerland.*

* These authors contributed equally.
† Corresponding author: luca.castiglioni@physik.uzh.ch

1. Detailed experimental methods

A Ti:sapphire based chirped-pulse amplification system provides ultrashort laser pulses (~25 fs, 1.2 mJ, central wavelength 796 nm) at 1 kHz repetition rate. These pulses are compressed to 7-12 fs by filament compression [1] in two Ar gas cells. The beam is then split into a probe branch (20%) that is sent through a delay line and a pump branch (80%), which produces attosecond pulse trains (20-45 eV, 300 as pulse width) by high-harmonic generation in Ar. After generation of the APT the residual IR and lower-order harmonic radiation is blocked by a 100 nm Al filter. Pump and probe beams are collinearly recombined by means of a drilled mirror; the harmonic radiation passes from behind through the centre hole (diameter 2 mm) of the mirror while the IR probe field is reflected on the front part. A gold-coated toroidal mirror (incidence angle 82°) focuses the two beams in front of a time-of-flight (ToF) spectrometer. Photoemission spectra from Ar gas are recorded at different delays between the two pulses (typical delay step = 250 as). The collection of these spectra constitutes the first RABBITT trace that was used for calibration purpose.

A second toroidal mirror (incidence angle 80°) images the first focus onto a solid sample surface in a one-to-one geometry. Photoemission spectra from the metal surface are recorded with a hemispherical electron analyser. These spectra are measured simultaneously with the ones in Ar and form the second RABBITT trace. Efficient differential pumping kept the pressure in the surface chamber below 7×10^{-10} mbar during the measurements, which allowed for prolonged acquisition without degradation of the surface by contamination. Ag(111) and Au(111) single crystals were cleaned by cycles of sputtering and annealing and the surface quality was verified by XPS and LEED. The propagation phase between the two foci was determined experimentally by performing a simultaneous RABBITT experiment with two Ar targets. All measurements were conducted at room temperature and a bias voltage of -5.00 V with respect to the analyzer was applied to the solid sample. The intensity settings for the simultaneous scans were optimized for the surface with a focus on clear SB contrast. Reasonable modulation contrast in the SB signal was obtained with an incidence angle of 75°. All data presented in this work were recorded at this incidence angle. Both pulses are *p*-polarized and the angle of incidence on the surface is 75°.

2. Data analysis

2.1 Extraction of spectral phase and photoemission delays

In a RABBITT measurement the oscillatory component of the sideband *2q* is:

$$S_{2q}(t) \sim \cos(2\omega t - \phi_{2q}), \quad \textbf{(1)}$$

where ω is the angular velocity of the IR driving field, t is the delay between the two pulses and q is a positive integer number. The temporal information about the system and the group delay of the harmonic radiation is encoded in the phase ϕ_{2q}. In a first step, this phase is retrieved from the experimental RABBITT trace. Subsequently, the contributions from photoemission dynamics and group delay of the harmonic radiation are disentangled.

Our RABBITT scans were recorded with relatively short (7-12 fs) probe pulses and, as a result, the region showing detectable sidebands only covered few laser cycles. A combination of Fourier analysis and curve fitting was applied to retrieve the experimental phase, ϕ_{2q}, of the sidebands. The signal integrated over the energy range specific to the sideband was Fourier filtered with a Gaussian window of 50 THz width. The peak in the Fourier spectrum of the simultaneously recorded scan in argon was chosen as central frequency. A time-domain filter (super-Gaussian of order 4) and zero padding prior to the Fourier transformation improved the spectral resolution.

For the surface RABBITT scan, instabilities in the XUV flux were removed by subtracting the average surface spectrum weighted by the total counts of the gas spectrum at the given delay. The number of electrons ionized in the gas phase does not depend on the IR field and presents a convenient measure for the flux in the XUV pulse. The filtered (and background subtracted) signal was fitted with the following five-parameter function, both in gas phase and on the surface:

$$S(t) = p_0 e^{p_1 (t-p_2)^2} \cos(2\pi p_3 t - p_4) \cdot \quad \textbf{(2)}$$

p_i denote the fitting parameters with p_4 representing the phase, ϕ_{2q}, of the corresponding sideband and p_3 being twice the central frequency obtained from the Fourier spectrum. It should be noted that the phase, ϕ_{2q}, could also be retrieved by direct curve fitting without Fourier filtering. In this case a modified fitting function was used that also accounts for a constant background and other contributions to the total signal. The results from both methods agree well within experimental uncertainty.

We performed Fourier analysis of the RABBITT traces to exclude higher-order contributions to the spectral phase. No indication of such higher-order processes can be seen in these spectra (Fig. S1).

Since the sideband oscillation is caused by the interference of two quantum paths, the extracted phase corresponds to the phase difference of these quantum paths and an unknown offset phase. This is written as

$$\phi_{2q}^{g/s} = \theta_{2q+1}^{1/2} + \varphi_{2q+1}^{g/s} + \varphi_{cc,2q+1}^{g/s} - (\theta_{2q-1}^{1/2} + \varphi_{2q-1}^{g/s} + \varphi_{cc,2q-1}^{g/s}) - 2\phi_0^{1/2} \cdot \quad \textbf{(3)}$$

θ is the phase of the harmonic radiation, φ is the system specific dipole transition phase and φ_{cc} denotes the measurement induced phase caused by the additional IR transition [2, 3]. The subscripts refer to the harmonic order, the superscripts to the target (g=gas, s=surface) or the site (1st and 2nd focus) of the measurement. The offset phase $\phi_0^{1/2}$ relates to the choice of $\tau = 0$, which is not experimentally accessible with required accuracy. Rearranging terms and omitting superscripts in the previous equation yields

$$\begin{aligned} \phi_{2q} &= (\theta_{2q+1} - \theta_{2q-1}) + (\varphi_{2q+1} - \varphi_{2q-1}) + (\varphi_{cc,2q+1} - \varphi_{cc,2q-1}) - 2\phi_0 \\ &= \Delta\theta_{2q} + \Delta\varphi_{2q} + \Delta\varphi_{cc,2q} - 2\phi_0 \\ &= 2\omega \cdot (\tau_{GD,2q} + \tau_\lambda + \tau_{cc} - \tau_0). \end{aligned} \quad \textbf{(4)}$$

τ_{GD} is the group delay of the high harmonic radiation, τ_λ the (single-photon) photoemission delay, τ_{cc} the continuum-continuum delay caused by the probe field [3] and τ_0 the time-shift corresponding to the offset phase. Since the sideband phase measured in RABBITT corresponds to a finite-difference approximation of the group delay at the sideband energy, the link between the phases and attributed delays becomes apparent. 2ω is the frequency separation of two neighboring sidebands. In the case of the calibration measurement in argon, the quantities τ_λ and τ_{cc} in Eq. (4) are known from literature [3, 4] .

2.2 Propagation and reflection phase

Care has to be taken when applying this calibration to the scan on the surface. The two measurements are conducted at different sites and the two pulses acquire additional phases during propagation between the two foci of the apparatus. This situation is indicated by the superscripts 1 and 2 in Eq. (3). The difference of the experimental phases in focus 1 and focus 2 can be written as follows:

$$\begin{aligned}\phi_{2q}^{(2)} - \phi_{2q}^{(1)} = \Delta\theta_{2q} + \Delta\theta_{2q}^{toro} + \Delta\varphi_{2q}^{(2)} + \Delta\varphi_{cc,2q}^{(2)} \\ -2\phi_0^{(2)} - (\Delta\theta_{2q} + \Delta\varphi_{2q}^{(1)} + \Delta\varphi_{cc,2q}^{(1)} - 2\phi_0^{(1)}).\end{aligned} \quad \textbf{(5)}$$

Since both IR and XUV beams propagate in vacuum their phase is only affected by the reflection on the toroidal mirror as well as the Gouy phase in the focus. $\Delta\theta_{2q}^{toro}$ accounts for the propagation phase of the XUV pulse. The offset phase, $\phi_0^{(2)}$, comprises all phases accumulated by the IR pulse between 1st and 2nd focus and is given by

$$\phi_0^{(2)} = \phi_0^{(1)} + \phi_{prop}^{IR} + \phi_{refl}^{IR}. \quad \textbf{(6)}$$

Noble metal surfaces are highly reflective in the IR and the probe field constitutes a transient grating[5] formed by the superposition of the incoming and reflected IR pulses with an associated phase ϕ_{refl}^{IR}.

Whereas the reflection phase of the toroidal mirror can be calculated using Fresnel's equations it is rather delicate to compute the Gouy phase. Hence we determined the propagation phase between the two foci experimentally. For this purpose a gas target was installed in the surface chamber at the position where the solid sample was placed normally. This enabled us to simultaneously record RABBITT traces of Ar in the 1st and 2nd focus. Invoking Eq. (5) we see that if we take the difference of the acquired phases we are left only with $\phi_{2q}^{(2)} - \phi_{2q}^{(1)} = 2\phi_0^{(1)} + \Delta\theta_{2q}^{toro} - 2\phi_0^{(2)}$. With a gas target in focus 2 there is no reflection on the surface and thus $\phi_{refl}^{IR} = 0$. We can therefore derive an experimental propagation phase:

$$\phi_{prop,2q} = \phi_{2q}^{(2)} - \phi_{2q}^{(1)} = \Delta\theta_{2q}^{toro} - 2\phi_{prop}^{IR}. \quad \textbf{(7)}$$

Any remaining energy dependence of the propagation phase must be attributed to the reflection of the XUV on the toroidal mirror since the intrinsic harmonic phases cancel out each other. Delays due to the reflection phase of the XUV in the region of 25-35 eV were computed to be more than two orders of magnitudes smaller than our experimental delays. This allowed us to use an energy-independent mean propagation phase, ϕ_{prop}, which is indicated by the blue line in Fig. S2.

In order to establish the relation between the offset phases $2\phi_0^{(1)}$ and $2\phi_0^{(2)}$ for surface RABBITT measurements we must assess ϕ_{refl}^{IR}. We compute the phase of the transient grating due to reflection on the surface based on Fresnel's equations. For parallel polarization the complex reflection coefficient for photon energy ε and angle of incidence θ is computed as

$$r_p(\epsilon) = \frac{\tilde{n}(\epsilon)^2 cos\theta - \sqrt{\tilde{n}(\epsilon)^2 - sin^2\theta}}{\tilde{n}(\epsilon)^2 cos\theta + \sqrt{\tilde{n}(\epsilon)^2 - sin^2\theta}}, \quad \textbf{(8)}$$

with complex refractive index $\tilde{n}$. Material data for $\tilde{n}$ were taken from Palik[6]. The Fresnel reflection phase of the IR, ϕ_{Fres}^{IR}, is directly given by the phase of expression (8):

$$\phi_{Fres}^{IR} = \arg(r_p(\varepsilon)) \quad \textbf{(9)}$$

The phase modulation introduced by the 2D-transient grating was computed as a function of the incident angle θ of the IR beam and the final momentum of the photoelectrons. Our simulations show that electrons with different directions are affected differently by the transient grating. The effective phase of the IR field felt by electrons with final direction in the detection cone of the analyzer (between 25° and 35° with respect to the surface normal) can be written as

$$\phi_{refl}^{IR} = \phi_{Fres}^{IR} / \beta \,, \tag{10}$$

where the parameter β = 1.70 was extracted from simulations taking the specific experimental geometry into account. The simulated transient grating is illustrated in Fig. S3.

2.3 Calibrated photoemission delays

All propagation-related phases being assessed, the relationship between corresponding quantities at the different measurement sites can be established. The difference of the experimental phases in focus 1 (gas) and focus 2 (surface) can be rewritten as follows:

$$\phi_{2q}^{s} - \phi_{2q}^{g} = \Delta\varphi_{2q}^{s} + \Delta\varphi_{cc,2q}^{s} - \Delta\varphi_{2q}^{g} - \Delta\varphi_{cc,2q}^{g} + \phi_{prop} - 2\phi_{refl}^{IR} \tag{11}$$

Finally the (two-photon) photoemission delay for the metal surface is obtained by taking the difference, $\phi_{2q}^{s} - \phi_{2q}^{g}$, making the link between phases and attributed delays according to Eq. (4) and rearranging the terms:

$$\begin{aligned} \tau_{2q}^{s} &= \tau_{\lambda,2q}^{s} + \tau_{cc,2q}^{s} + \tau_{trans}^{s} \\ &= \frac{\phi_{2q}^{s} - \phi_{2q}^{g}}{2\omega} + \tau_{\lambda,2q}^{g} + \tau_{cc,2q}^{g} - \tau_{prop} + \tau_{refl}. \end{aligned} \tag{12}$$

The resulting delay, τ_{2q}^{s}, is the sum of all processes that contribute to the photoemission from a metal in the RABBITT process, namely a Wigner-type one-photon delay, τ_{λ}^{s}, a contribution from transport, τ_{trans}, as well as an additional delay, τ_{cc}^{s}, resulting from the continuum-continuum interaction with the IR probe field.

3. Simulation of photoemission delays

3.1 Calculation of Wigner delays and τ_{cc}

The Wigner delay arises from the initial excitation by the XUV pulse out of *4d* and *5d* bands in Ag and Au, respectively. This delay originates from the phase of the outgoing intermediate state $|\vec{k}\rangle$ as compared to a plane wave of same wavevector and can be calculated as scattering phase of half an elastic scattering event since photoemission can be considered a half collision. Phase shifts and radial matrix elements were calculated using the Linearized Muffin-Tin Orbital (LMTO) method [7]. For the excitation, dipole selection rules are assumed, *i.e.* excitation into outgoing spherical harmonics of l=1 and l=3. The coherent superposition of *p*- and *f*-states yields the phase of state $|\vec{k}\rangle$.

The amplitudes of the transition into *p*- or *f*-states, respectively, are calculated by evaluating the transition matrix elements of initial and final states. The time delay associated with the phase is obtained by

$$\tau_{Wigner} = \hbar \frac{d\varphi}{dE} \,. \tag{13}$$

The interaction of the intermediate state with the IR field described by the transition $|\vec{k}\rangle \rightarrow |\vec{k}'\rangle$ leads to τ_{cc}. Similar to the computation of the Wigner delay described above, the sum of the two half-scattering phases yields the phase shift of a partial wave due to the continuum-continuum transition. The incoming wave (from photoemission from *d* states) is of *p*- or *f*-character with the amplitudes given by the initial excitation, *i. e.* the radial matrix elements calculated within the LMTO scheme [7]. All contributions were summed up coherently as different magnetic quantum numbers are not distinguished in the experiment.

The total continuum-continuum contribution to the delay is then given by

$$\tau_{cc} = \frac{\varphi_{>} - \varphi_{<}}{2\omega} \,. \tag{14}$$

Here $\varphi_{>}$ and $\varphi_{<}$ are the phases along two different quantum paths (absorption and stimulated emission) that lead to the same sideband and are obtained by recurring the following formula for all partial wave phase shifts:

$$\tan(\varphi'_{<}) = \frac{A_{ps}\cdot\sin(\delta_{p\to s}) + A_{pd}\cdot\sin(\delta_{p\to d})}{A_{ps}\cdot\cos(\delta_{p\to s}) + A_{pd}\cdot\cos(\delta_{p\to d})}, \quad \textbf{(15)}$$

with

$$\delta_{p\to s}(E_{SB}) = \delta_p(E_{SB}+\hbar\omega) + \delta_s(E_{SB}) \quad . \quad \textbf{(16)}$$

$\delta_{i\to j}$ denote respective photoemission phase shifts. φ' in Eq. (15) is the phase of the coherent superposition of partial waves *s* and *d*. To coherently superimpose this wave with the next allowed partial wave following path *f* to *d* Eq. (15) is recurred. The recursion is repeated until all partial waves are summed up to yield one wave with phase $\varphi_{<}$.

3.2 Calculation of transport times

Transport times were modeled based on ballistic transport in the intermediate state after the XUV excitation. The transition momenta (assuming direct transitions due to negligible photon momenta) are obtained from the momentum of the photoelectron in vacuum. Using the formulas below for the refraction at the surface, the momentum in the crystal can be calculated:

$$k_{\parallel} = \sqrt{\frac{2m^*}{\hbar^2}\left(\hbar\omega_{XUV} - E_B - \phi\right)}\cdot\sin(\Theta) \quad \textbf{(17)}$$

$$k_{\perp} = \sqrt{\frac{2m^*}{\hbar^2}\left[\left(\hbar\omega_{XUV} - E_B - \phi\right)\cdot\cos^2(\Theta) - V_0\right]} \quad \textbf{(18)}$$

V_0 is the inner potential with respect to the vacuum level, Θ the emission angle with respect to the surface normal (111), m^* the effective mass of the final state band, and ϕ the work function of the samples.

	Ag(111)	Au(111)
m^*	m_e	m_e
V_0 (eV)	-12.24	-14.4
ϕ (eV)	4.74	5.4
V_0 (eV)	-5	-4
Θ (deg)	30	30

Table S1. Values for Eqs (17) and (18) taken from Refs [8, 9].

The group velocity is obtained from fits of free-electron final states to the bulk band structure using the inner potentials and effective masses given in Tab. S1. The group velocity obtained is given by the derivative:

$$v_g = \hbar^{-1}\frac{\partial E(k)}{\partial k} \approx 30 \text{ Å/fs} \quad \textbf{(19)}$$

The (screened or unscreened) hydrogen-like potential of the photohole was included such that the wave vector and group velocities were evaluated numerically as a function of distance from the site of the XUV excitation. The potential was of the form

$$V_{PH}(r) = \frac{-e^2}{4\pi\varepsilon_0 r}\cdot e^{-r/l_{TF}} \quad \textbf{(20)}$$

with the Thomas-Fermi length, l_{TF}, of 0.5 Å for silver and 0.2 Å for gold [10]. In the case of the unscreened potential the exponential factor was set to 1.

Integration over the path length yields an effective transport time. The typical time scale of the build-up of screening is predicted to be in the range of 250 as [11], and hence in the range of our experiments. Since the actual time scale is unknown the transport was evaluated once for a completely screened and once for an unscreened photohole potential.

References

1. C. P. Hauri, W. Kornelis, F. W. Helbing, A. Heinrich, A. Couairon, A. Mysyrowicz, J. Biegert, and U. Keller, "Generation of intense, carrier-envelope phase-locked few-cycle laser pulses through filamentation," Appl. Phys. B **79**, 673-677 (2004).
2. K. Klünder, J. M. Dahlström, M. Gisselbrecht, T. Fordell, M. Swoboda, D. Guenot, P. Johnsson, J. Caillat, J. Mauritsson, A. Maquet, R. Taïeb, and A. L'Huillier, "Probing Single-Photon Ionization on the Attosecond Time Scale," Phys. Rev. Lett. **106**, 143002 (2011).
3. J. M. Dahlström, D. Guénot, K. Klünder, M. Gisselbrecht, J. Mauritsson, A. L'Huillier, A. Maquet, and R. Taïeb, "Theory of attosecond delays in laser-assisted photoionization," Chem. Phys. **414**, 53-64 (2013).
4. J. Mauritsson, M. B. Gaarde, and K. J. Schafer, "Accessing properties of electron wave packets generated by attosecond pulse trains through time-dependent calculations," Phys. Rev. A **72**, 013401 (2005).
5. U. Bovensiepen, S. Declair, M. Lisowski, P. A. Loukakos, A. Hotzel, M. Richter, A. Knorr, and M. Wolf, "Ultrafast electron dynamics in metals: Real-time analysis of a reflected light field using photoelectrons," Phys. Rev. B **79**, 045415 (2009).
6. E. D. Palik, *Handbook of Optical Constants of Solids* (Academic Press, 1985).
7. O. K. Andersen, Z. Pawlowska, and O. Jepsen, "Illustration of the linear-muffin-tin-orbital tight-binding representation: Compact orbitals and charge density in Si," Phys. Rev. B **34**, 5253-5269 (1986).
8. S. Hüfner, *Photoelectron Spectroscopy* (Springer, Berlin, 2003).
9. H. Eckardt, L. Fritsche, and J. Noffke, "Self-consistent relativistic band structure of the noble metals," Journal of Physics F: Metal Physics **14**, 97 (1984).
10. A. B. Buckman and N. M. Bashara, "Electroreflectance Changes in Dielectric Constants of Au and Ag by Modulated Ellipsometry," Phys. Rev. **174**, 719-721 (1968).
11. R. D. Muiño, D. Sánchez-Portal, V. M. Silkin, E. V. Chulkov, and P. M. Echenique, "Time-dependent electron phenomena at surfaces," Proc. Nat. Acad. Sci. **108**, 971-976 (2011).

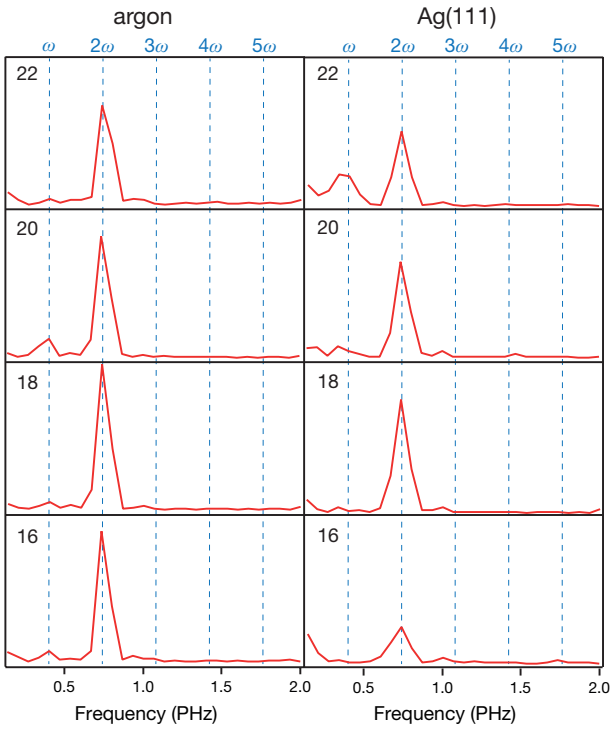

Fig. S1. Normalised power spectra of the Fourier analysis of the sideband modulation in argon and Ag(111). The number of the harmonics and frequencies as integer multiples of the fundamental IR frequency are indicated. The 2ω signal is the modulation of the RABBITT process.

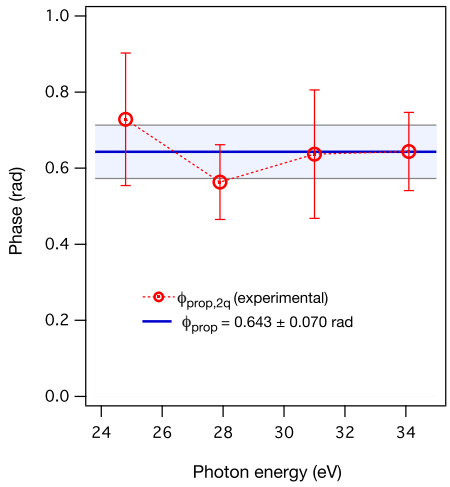

Fig S2. Propagation phase derived from RABBITT measurements in two Ar targets at the two different foci. The blue shaded area indicates the standard deviation of the mean phase.

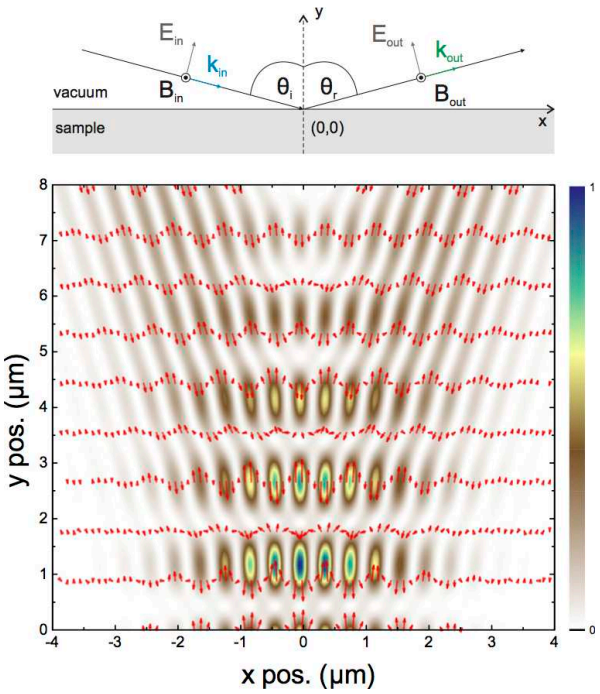

Fig. S3. Two-dimensional transient grating due to reflection of the IR pulse at the sample surface at instant $\tau = 0$ fs. The colour scale on the right displays the intensity of the electric field, the amplitude is indicated by the red arrows. The top scheme illustrates the vectors describing the IR pulse and the sign convention used in our calculations.